RSC Advances

PAPER

View Article Online
View Journal | View Issue

Cite this: *RSC Adv.*, 2018, **8**, 37200

Visible-light-driven Ag/Bi_3O_4Cl nanocomposite photocatalyst with enhanced photocatalytic activity for degradation of tetracycline

Enhui Jiang,†[a] Xiaoteng Liu,†[b] Huinan Che,[a] Chunbo Liu,[b] Hongjun Dong[b] and Guangbo Che*[c]

In this study, a novel Ag/Bi_3O_4Cl photocatalyst has been synthesized by a facile photodeposition process. Its photocatalytic performance was evaluated from the degradation of tetracycline (TC) under visible light irradiation (λ > 420 nm). The 1.0 wt% Ag/Bi_3O_4Cl photocatalyst could significantly enhance the degradation of TC compared with pure Bi_3O_4Cl, with the degradation level reaching 94.2% in 120 minutes. The enhancement of photocatalytic activity could be attributed to the synergetic effect of the photogenerated electrons (e^-) of Bi_3O_4Cl and the surface plasmon resonance (SPR) caused by Ag nanoparticles, which could improve the absorption capacity of visible light and facilitate the separation of photogenerated electron–hole pairs. In addition, electron spin resonance (ESR) analysis and trapping experiments demonstrated that the superoxide radicals ($^{\bullet}O^{2-}$), hydroxyl radicals ($^{\bullet}OH$) and holes (h^+) played crucial roles in the photocatalytic process of TC degradation. The present work provides a promising approach for the development of highly efficient photocatalysts to address current environmental pollution, energy issues and other related areas.

Received 7th September 2018
Accepted 17th October 2018

DOI: 10.1039/c8ra07482h

rsc.li/rsc-advances

1. Introduction

Antibiotics, as one of the most significant medicines, have been immoderately applied in our lives in agriculture, medicine and planting, and are frequently detected in a wide range of environmental samples, including treated wastewater and even drinking water.[1–4] Furthermore, the very low concentration of antibiotic solutions might lead to the appearance of drug resistance among pathogenic microbes, and even generate multiple-resistances in human beings. The abuse of tetracycline (TC) is particularly serious.[5–8] Moreover, the elimination of TC cannot be achieved by the natural environment itself or by sewage treatment plants.[9,10] Therefore, exploring an effective method for eliminating TC from sewage has become an exigency. Recently, several approaches have been explored for the removal of TC from our environment, such as electrochemistry, precipitation, adsorption and photocatalysis. Among these, photocatalysis has been proven to be a promising environmentally-friendly technology for removing TC from the sewage because it can take advantage of green and sustainable solar energy, it is non-poisonous, and photocatalysts can have stable properties. So far, research into the degradation of TC by TiO_2,[11] CdS,[12] $SrTiO_3$ (ref. 13) and Ag_2O (ref. 14) photocatalysts has been instigated by several researchers. However, the practical applications of these materials are limited due to the rapid recombination rates of the electron–hole pairs, poor stability, and the low use efficiency of solar energy. Therefore, it is imperative to overcome the above shortcomings and explore novel photocatalysts which offer high degradation efficiencies for TC under visible light irradiation.

Nowadays, bismuth oxyhalides (BiOX, X = Cl, Br, and I) as a class of layered semiconductor materials have become prevalent as photocatalysts on account of their unique and excellent electrical properties, suitable energy band positions and high-efficiency photocatalytic activities.[15–18] In particular, Bi_3O_4Cl has a layered Sillén-Aurivillius-related oxide structure consisting of [Bi_3O_4] layers sandwiched between two slabs of [Cl] ions in an extraordinarily open crystalline structure.[19,20] On account of the distinctive crystalline structure, there is a self-built internal static electric field to facilitate the separation and transportation of photogenerated electrons and holes to improve the photocatalytic performance.[21] However, unfortunately, the use of Bi_3O_4Cl is constrained by its weak visible light absorption and low rate of charge transfer when applied in practice. Therefore, it is important to improve the photocatalytic performance of the single Bi_3O_4Cl photocatalyst.

Recently, noble metals such as Au, Pt and Ag have captured considerable attention due to their splendid conductivity and

[a]*School of Chemistry and Chemical Engineering, Jiangsu University, Zhenjiang, 212013, P. R. China*

[b]*Institute of Green Chemistry and Chemical Technology, School of Chemistry and Chemical Engineering, Jiangsu University, Zhenjiang, 212013, P. R. China*

[c]*Key Laboratory of Preparation and Application of Environmental Friendly Materials, Jilin Normal University, Ministry of Education, Changchun 130103, P. R. China. E-mail: guangboche@jlnu.edu.cn; Fax: +86 511 8879 1108; Tel: +86 511 8879 0885*

† Enhui Jiang and Xiaoteng Liu are co-first authors.

capacity for trapping electrons. In particular, Ag is fairly cheap and exhibits intense local electromagnetic fields caused by surface plasmon resonance (SPR), which can expedite the separation of electron–hole pairs within a semiconductor and improve the absorption of visible light.[22–24] In recent years, Luo's team has reported that the Ag/Bi_3TaO_7 plasmonic photocatalyst exhibited a more excellent photocatalytic performance than pure Bi_3TaO_7 for the degradation of TC under visible light, which was due to the SPR which facilitated the efficient separation of photogenerated electron–hole pairs and enhanced the absorption of visible light.[25] To date, however, there has been no work reported on the synthesis of an Ag/Bi_3O_4Cl photocatalyst for the efficient degradation of TC under visible light.

In this work, Ag/Bi_3O_4Cl photocatalysts were synthesized by a facile photodeposition process with different contents of silver nitrate. The photocatalytic activities of the Ag/Bi_3O_4Cl photocatalysts were measured by the degradation of TC under visible light irradiation. Among these samples, the 1.0 wt% Ag/Bi_3O_4Cl photocatalyst showed outstanding photocatalytic activity. Moreover, the separation and migration of photogenerated charge carriers were evaluated by photocurrent and electrochemical impedance spectroscopy (EIS) analysis. Furthermore, active species trapping experiments and the electron spin resonance (ESR) technique were used to analyze the possible mechanism for the enhanced photocatalytic process.

2. Experimental

2.1. Materials

$Bi(NO_3)_3 \cdot 5H_2O$, NH_4Cl, $AgNO_3$, disodium ethylene-diamine tetraacetate (EDTA-2Na), tertiary butanol (TBA), ascorbic acid (VC), ethanol, and ethanediol were purchased from Aladdin (Shanghai, China). They were of analytical grade and were used as received from the commercial supplier without further purification.

2.2. Preparation of photocatalysts

Bi_3O_4Cl nanosheets were prepared by the following hydrothermal method based on the literature report.[26] $Bi(NO_3)_3 \cdot 5H_2O$ (1 mmol) (≥98%, Aldrich) was dispersed in 10 mL ethanediol with vigorous sustained magnetic stirring at 2000 rpm for 30 min. Subsequently, 25 mL NH_4Cl (0.34 mmol) solution was added and a white slurry formed immediately. Thereafter, the resultant mixture was transferred into a 50 mL Teflon-lined stainless-steel autoclave with high-temperature resistance and maintained at 160 °C for 12 h. A white precipitate formed after the entire system cooled naturally to room temperature. The product was collected centrifugally and washed three times with deionized water and absolute ethanol. Then the obtained product was dried at 60 °C in the oven overnight. Finally, the yellow product was formed after the white precipitate was transferred into porcelain boats and annealed at 550 °C for 5 h in a muffle furnace at a heating rate of 5 °C min^{-1}.

The Ag/Bi_3O_4Cl photocatalysts were prepared by the method of photodeposition. In a typical reaction, 0.5 g Bi_3O_4Cl powder was dispersed in 1 mg mL^{-1} $AgNO_3$ solution (volume determined from the required proportion of Ag). The suspension was stirred for 30 min, and then exposed to a 250 W xenon lamp for 1 h, as shown in Fig. 1. Thereafter, the as-prepared Ag/Bi_3O_4Cl samples were obtained by centrifugation. In order to eliminate the adsorbed silver ions (Ag^+), the eventual products were washed three times with deionized water. Finally, the as-prepared samples were dried in the oven at 60 °C overnight. The proportions of Ag were 0, 0.5 wt%, 1.0 wt%, 3.0 wt% and 5.0% (weight percent).

2.3. Characterizations

The X-ray diffraction (XRD) patterns of the as-prepared samples were obtained by using a Rigaku D/MAX-2500 diffractometer (Cu Kα radiation, $\lambda = 0.1542$ nm) with a scanning speed of 5° min^{-1} in the 2θ range of 10–80°. The energy dispersive X-ray spectroscopy (EDX) images were collected with an accelerating voltage of 200 kV (SEM, Hitachi) with a F20 S-TWIN electron microscope (Tecnai G2, FEI Co.). The transmission electron microscopy (TEM) and high-resolution TEM (HRTEM) images were collected using a F20 S-TWIN electron microscope, operated at 200 kV (Tecnai G2, FEI Co.) to obtain the chemical states of the photocatalysts. UV-vis diffuse reflectance spectroscopy (DRS) of the photocatalysts was performed using a UV-vis spectrophotometer (UV-2450, Shimadzu, Japan). The electron spin resonance (ESR) spectra were detected by using a Bruker EPR A 300-10/12 spectrometer to measure the activated species. Photocurrents were obtained and electrochemical impedance spectroscopy (EIS) was conducted using a CHI 760D electrochemical workstation.

2.4. Photocatalytic activity tests

The photocatalytic activities of the as-prepared samples were estimated by monitoring the degradation of TC under visible light irradiation. The light source was a 250 W xenon lamp with a 420 nm cutoff filter. In a typical photocatalytic experiment, 50 mg of sample was dispersed in an aqueous solution of 100 mL TC (10 mg L^{-1}) in a photochemical reactor. Prior to the bright irradiation, the suspension was stirred in the dark for 30 min to achieve an adsorption–desorption equilibrium between the photocatalyst and TC. During the photocatalytic reaction, 5 mL samples of the suspension were removed at 20 min intervals and centrifuged to obtain the supernatants. The concentration of TC in each solution was measured by UV-

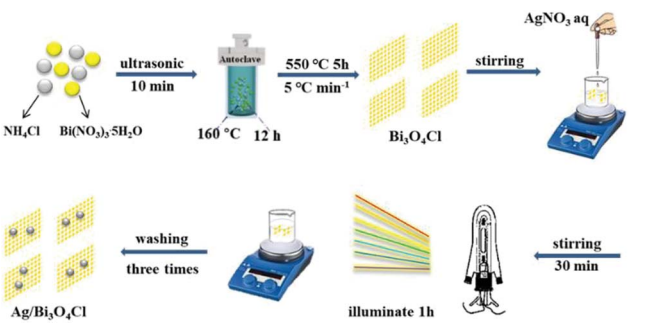

Fig. 1 Synthesis process for the Ag/Bi_3O_4Cl photocatalyst.

vis spectroscopy using the absorbance at the characteristic band of 357 nm. The efficiency of degradation was calculated by using C/C_0, in which C is the concentration of the reactants at a certain irradiation time and C_0 is the original concentration.

2.5. Kinetic study of TC decomposition

To further comprehend the degradation process, the photocatalytic degradation kinetics were researched using the Langmuir–Hinshelwood (L–H) model which can be calculated by the following equation:[27–30]

$$\ln(C_0/C) = k_{app}t$$

in which C_0, C and k are the adsorption equilibrium concentration, TC concentration at a certain irradiation time (t), and the apparent reaction rate constant (inverse minutes), respectively.

2.6. Photoelectrochemical measurements

Photocurrent and EIS tests were carried out using a CHI 760D electrochemical workstation in a standard three-electrode configuration with an as-prepared sample as the working electrode, a Pt plate as the counter electrode and an Ag/AgCl electrode as the reference electrode. The electrolyte was a 0.5 mol L^{-1} Na_2SO_4 aqueous solution. Each working electrode was prepared as follows: 0.03 mL oleic acid, 0.01 g polyvinyl pyrrolidone (PVP) and 0.03 g sample were dispersed in 3 mL ethanol with stirring for 30 min to make a slurry. The mixture was then spin coated onto a 15 mm × 20 mm indium–tin oxide (ITO) coated glass, and the working electrode was heated in a drying oven at 60 °C for 2 h. A 300 W xenon lamp served as the visible light source (λ > 420 nm).

2.7. Active species trapping experiments

Radical scavengers were employed in order to identify the active species during the photocatalytic process of TC degradation under visible light irradiation. Ascorbic acid (VC) was used to capture $^{\bullet}O^{2-}$ radicals, isopropyl alcohol (IPA) was used for $^{\bullet}OH$ radicals and disodium ethylene-diamine tetraacetate (EDTA-2Na) was used for h^+.[31–33] The concentrations of scavengers were all 1 mM, and the experiments followed the process described for the photocatalytic activity test. Furthermore, ESR technology was used to search for the existence of $^{\bullet}O^{2-}$ and $^{\bullet}OH$ radicals in the photocatalytic reaction system under visible light irradiation (λ > 420 nm). Samples for ESR measurement were prepared as follows: 10.0 mg sample was dissolved in 0.5 mL methanol, and 45 μL DMPO was added with ultrasonic dispersion for 5 min to form DMPO – $^{\bullet}O^{2-}$; 0.5 mL deionized water was used in place of methanol to form DMPO – $^{\bullet}OH$.[34,35]

3. Results and discussion

3.1. Structure and composition

The crystalline structures of the as-prepared samples were revealed by the X-ray diffraction (XRD) analysis. Fig. 2a shows the XRD patterns of the as-prepared pure Bi_3O_4Cl nanosheets and the Ag/Bi_3O_4Cl photocatalysts with different contents of Ag

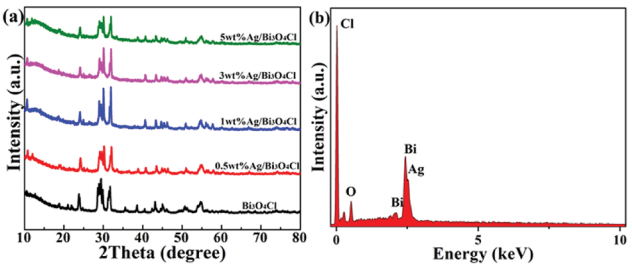

Fig. 2 (a) XRD patterns of Bi_3O_4Cl and Ag/Bi_3O_4Cl samples. (b) EDX spectrum of the 1 wt% Ag/Bi_3O_4Cl photocatalyst.

(0.5 wt%, 1.0 wt%, 3.0 wt%, 5.0 wt%). For all samples, the characteristic peaks could be indexed to the monoclinic phase of Bi_3O_4Cl (JCPDF No. 36-0760).[26] Peaks of the Ag phase were not detected which is probably due to the quite low contents of Ag. In addition, the elemental composition of the Ag/Bi_3O_4Cl photocatalyst (1 wt%) was detected by EDX. As shown in Fig. 2b, the elements of Bi, Cl, O and Ag were found in the Ag/Bi_3O_4Cl photocatalyst, indicating that the Ag nanoparticles had been deposited on the surface of the Bi_3O_4Cl nanosheets. Furthermore, the EDX showed that for the 1 wt% Ag/Bi_3O_4Cl photocatalyst, the atomic ratio of Bi : O : Cl was very close to 3 : 4 : 1 and the mass percent of Ag nanoparticles approached 1%. Obviously, the above results confirmed that the tested amounts were similar to the calculated values.

3.2. Microstructure analyses

To further affirm the successful deposition of the Ag nanoparticles on the Bi_3O_4Cl nanosheets, the morphologies and microstructures of the Bi_3O_4Cl nanosheets and 1 wt% Ag/Bi_3O_4Cl photocatalyst were characterized by SEM, TEM and HRTEM analysis. As shown in Fig. 3a and b, the SEM and TEM images of the pure Bi_3O_4Cl nanosheets exhibited sheet-like structures with clean and smooth surfaces. In contrast, the TEM images (Fig. 3c and d) of the 1 wt% Ag/Bi_3O_4Cl photocatalyst clearly showed nanoparticles with diameters of approximately 50 nm on the surface of the sample which

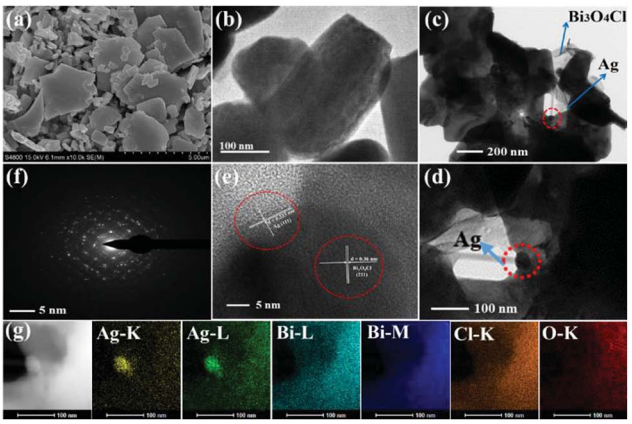

Fig. 3 (a) SEM and (b) TEM images of pure Bi_3O_4Cl nanosheets. (c and d) TEM, (e) HRTEM and (f) SAED images of the 1 wt% Ag/Bi_3O_4Cl photocatalyst. (g) HAADF-STEM image of the 1 wt% Ag/Bi_3O_4Cl photocatalyst.

illustrated that the Ag nanoparticles had been successfully deposited on the surface of the Bi_3O_4Cl nanosheets. Meanwhile, the HRTEM image of the 1 wt% Ag/Bi_3O_4Cl photocatalyst in Fig. 3e showed a lattice-fringe spacing of 0.36 nm ($d = 0.36$ nm) which corresponded to the (211) plane of the Bi_3O_4Cl nanosheets, and a spacing of $d = 0.233$ nm which matched well with the (111) plane of Ag nanoparticles. Additionally, Fig. 3f, which shows the SAED graphics with the typical dot patterns, indicated that the Bi_3O_4Cl nanosheets were composed of monocrystalline nanoparticles.[36] Furthermore, the high-angle annular dark-field scanning transmission electron microscopy (HAADF-STEM) patterns in Fig. 3g demonstrated that Bi, O, Cl, and Ag elements were distributed throughout the whole material, in accordance with the EDX analysis.

3.3. XPS analyses

To further research the surface composition and chemical oxidation state of the Ag/Bi_3O_4Cl photocatalyst, X-ray photoelectron spectroscopy (XPS) was conducted and the results are shown in Fig. 4a. It is worth noting that the XPS survey spectrum of the Ag/Bi_3O_4Cl photocatalyst displayed all the elements of Bi, O, Cl and Ag, which was in keeping with the EDX and HAADF-STEM results. Fig. 4b exhibits the Ag 3d spectrum; two characteristic peaks at 367.18 eV and 373.18 eV, with a 6 eV spin–orbit splitting value, suggested that the Ag species was present in the Ag/Bi_3O_4Cl photocatalyst system.[37–40] In addition, Fig. 4c (O 1s spectrum) shows that two different oxygen species presented on the surface of the as-prepared sample; the binding energy at 530.48 eV was due to the Bi–O bond and the peak at 529.1 eV was on account of the surface hydroxyl groups (Bi–O–H) in the samples. It was notable that the Cl 2p XPS spectrum in Fig. 4d displayed two peaks at 197.13 eV and 199.03 eV, which corresponded to the $2p_{3/2}$ and $2p_{1/2}$ orbitals of Cl^-, respectively. As shown in Fig. 4e, Bi 4f peaks at 163.58 eV and 158.28 eV were ascribed to Bi $4f_{5/2}$ and Bi $4f_{7/2}$, which were assigned to Bi^{3+} in the samples. The results suggested that the samples possessed Ag, Bi^{3+}, Cl^- and O^{2-} states coexisting in the Ag/Bi_3O_4Cl microcosmic architecture.[41]

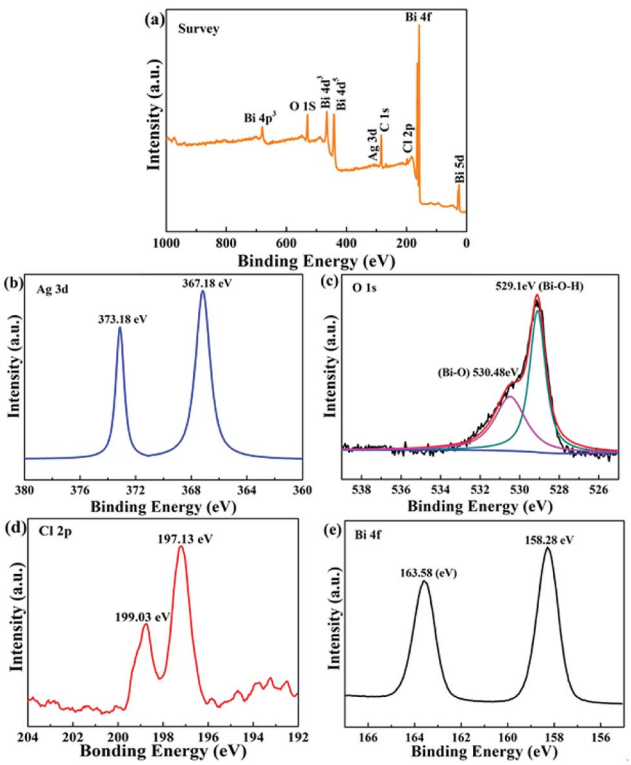

Fig. 4 XPS spectra of the 1.0 wt% Ag/Bi_3O_4Cl photocatalyst: (a) survey spectrum, and (b) Ag 3d, (c) O 1s, (d) Cl 2p, and (e) Bi 4f spectra.

3.4. UV-vis absorption spectra

The light absorption and energy band features of the as-prepared samples were examined by UV-vis diffuse reflectance spectroscopy (DRS). It was remarkable that the color of the as-prepared samples transformed from yellow to brown with increasing content of deposited Ag (Fig. 5a). Compared to pure Bi_3O_4Cl nanosheets, the as-prepared Ag/Bi_3O_4Cl photocatalysts showed an enhancement of photoabsorption in the visible light region owing to the SPR effect of the Ag nanoparticles.[42] In particular, the 1 wt% Ag/Bi_3O_4Cl photocatalyst displayed an excellent visible light absorption intensity, which implied that it more easily produced photogenerated charge carries which should improve its photocatalytic performance. Based on the absorption spectra, curves of converted $(\alpha h\nu)^n$ *versus* $h\nu$ were plotted and the equation $\alpha h\nu = A(h\nu - E_g)^{n/2}$ was used to calculate the band gap energies (E_g), where α, h, ν, A and E_g are the absorption coefficient, Planck constant, light frequency, proportionality constant and the band gap, respectively.[43] Importantly, the type of optical transitions of a semiconductor determines the value of n ($n = 1$ for indirect transitions and $n = 4$ for direct transitions), and, the value of n for Bi_3O_4Cl has been reported as 1 in previous literature reports.[36] As shown in Fig. 5b, it was obvious that the energy gap varied from 2.78 eV to 2.6 eV. The band gap of the Bi_3O_4Cl nanosheets showed a few changes after they were loaded with Ag nanoparticles, which might be because the metallic clusters introduced localized energy levels into the Bi_3O_4Cl band gap,[44] moreover, this change was one of the most important reasons for the enhanced degradation efficiency.

3.5. Photocatalytic tests

The photocatalytic activities of the as-prepared samples were measured by TC degradation under visible light illumination. It was found that TC in aqueous solution hardly degraded without

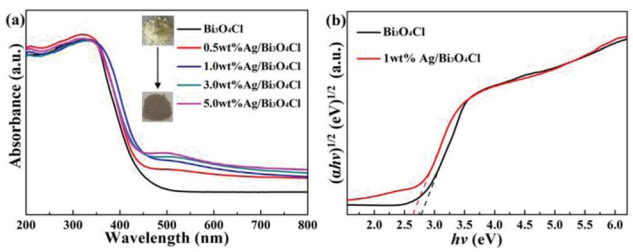

Fig. 5 (a) UV-vis DRS of the as-prepared samples. (b) Plots of $(\alpha h\nu)^{1/2}$ *versus* $h\nu$ for pure Bi_3O_4Cl nanosheets and the 1.0 wt% Ag/Bi_3O_4Cl photocatalyst.

the catalysts under visible light irradiation (Fig. 6a), so the blank experiment of the direct photolysis of TC showed a negligible effect. Compared to that of bare Bi_3O_4Cl nanosheets, the degradation efficiency was significantly enhanced after the deposition of Ag nanoparticles. Fig. 6a shows that the photocatalytic degradation efficiencies of TC were 61.5%, 70.3%, 94.2%, 75.2% and 73.8% for the bare Bi_3O_4Cl nanosheets, 0.5 wt% Ag/Bi_3O_4Cl, 1.0 wt% Ag/Bi_3O_4Cl, 3.0 wt% Ag/Bi_3O_4Cl and 5.0 wt% Ag/Bi_3O_4Cl, respectively. As shown in Fig. 6b, it was obvious that the optimal level of Ag deposition was 1.0% which gave the best degradation rate of 94.2%. Superfluous Ag nanoparticles might enshroud the surface of the samples and prevent the absorption of light leading to a reduction in the number of photogenerated electrons and holes in the Bi_3O_4Cl nanosheets; the nanoparticles might also take up a greater proportion of the active sites on the surface of the Bi_3O_4Cl nanosheets to reduce the surface adsorption capability of Bi_3O_4Cl for the TC molecules and reduce the photocatalytic activity. Notably, Fig. 6c shows that all the photodegradation data could be fitted well to the Langmuir–Hinshelwood model, which is associated with the pseudo-first-order kinetic correlation ($\ln(C/C_0) = k_{app}t$). As shown in Fig. 6d, the values of the reaction rate constants (k_{app}) of blank, pure Bi_3O_4Cl nanosheets, 0.5 wt% Ag/Bi_3O_4Cl, 1.0 wt% Ag/Bi_3O_4Cl, 3.0 wt% Ag/Bi_3O_4Cl and 5.0 wt% Ag/Bi_3O_4Cl nanocomposites were calculated to be 0.0000495, 0.00759, 0.00986, 0.0232, 0.0113 and 0.0108 min^{-1}, respectively. The rate constant of 1.0 wt% Ag/Bi_3O_4Cl was up to 3.05-fold greater than that of the bare Bi_3O_4Cl nanosheets.

3.6. Photocurrents and EIS analysis

The efficient separation of photogenerated electron–hole pairs could be demonstrated by the photocurrents which further illustrated the reason for the high photocatalytic activity of the photocatalysts. As shown in Fig. 7a, the intensity and stability of the photocurrent responses were enhanced when the as-prepared samples were used as electrodes under visible light illumination. Compared to the pure Bi_3O_4Cl nanosheets, the 1.0 wt% Ag/Bi_3O_4Cl photocatalyst displayed the highest photocurrent response, which illustrated that the introduction of the Ag nanoparticles efficiently enhanced the separation of photogenerated electron–hole pairs. Furthermore, the EIS electrochemical method effectively testified to the electron-transfer efficiency on the electrodes.[45–50] As is well-known, a smaller circular radius indicates a higher mobility and separation of photogenerated electron–hole pairs. It could be observed from the Nyquist plots (Fig. 7b) that 1.0 wt% Ag/Bi_3O_4Cl nanocomposites exhibited a smaller radius than any other sample, which suggested that the 1.0 wt% Ag/Bi_3O_4Cl photocatalyst had a resistance that was lower than those of the others and that it exhibited an excellent efficiency of charge transfer due to the modification with Ag nanoparticles.

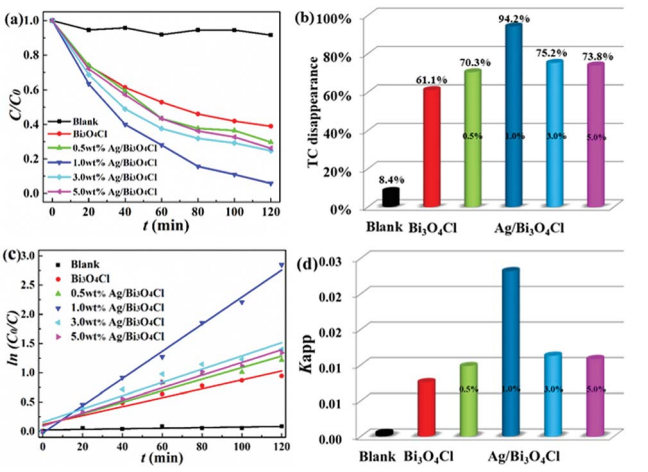

Fig. 6 (a) Photocatalytic degradation of TC with the as-prepared samples under visible light irradiation. (b) The levels of TC disappearance in the presence of the as-prepared samples. (c) Pseudo-first-order kinetic plots for the TC photodegradation with pure Bi_3O_4Cl nanosheets and Ag/Bi_3O_4Cl photocatalysts. (d) Reaction rate constants for the as-prepared samples.

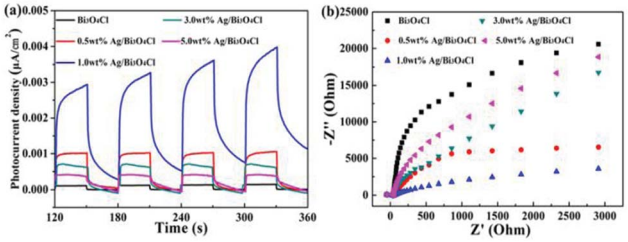

Fig. 7 (a) Photocurrent responses of the as-prepared samples. (b) EIS of the as-prepared samples.

3.7. Photocatalytic mechanism research

In order to confirm the main active substances responsible for TC degradation, free radical trapping experiments were implemented by adding various scavengers into the TC solution with the 1.0 wt% Ag/Bi_3O_4Cl photocatalyst. Scavengers of 1 mM ascorbic acid (VC), isopropyl alcohol (IPA) and disodium ethylene-diamine tetraacetate (EDTA-2Na) were used to capture $^{\cdot}O^{2-}$, $^{\cdot}OH$, and h^+, respectively. The photocatalytic efficiency of TC was affected by the addition of VC, IPA and EDTA-2Na (Fig. 8a and b). Therefore, $^{\cdot}O^{2-}$, $^{\cdot}OH$ and h^+ all played a vital role during the photocatalytic degradation of TC in the Ag/Bi_3O_4Cl photocatalyst system under visible light irradiation.

To further demonstrate the above conclusion, the ESR technique was used for detecting the presence of $^{\cdot}O^{2-}$ radicals and $^{\cdot}OH$ radicals in the as-prepared Ag/Bi_3O_4Cl photocatalyst reaction system. It can be clearly seen in Fig. 8c and d that four intense characteristic peaks for DMPO-$^{\cdot}O^{2-}$ adducts were observed (1 : 1 : 1 : 1 quartet pattern) under visible light irradiation, as well as signals for DMPO-$^{\cdot}OH$ radicals (1 : 2 : 2 : 1 quartet pattern);[51] the other four intense peaks are due to the oxidation of DMPO. Therefore, based on the above experimental results, $^{\cdot}O^{2-}$ radicals and $^{\cdot}OH$ radicals were identified as active oxidation species during the photodegradation process.

Photostability and recyclability are crucial factors in the practical application of a photocatalyst. The photostability and recyclability of the 1.0 wt% Ag/Bi_3O_4Cl photocatalyst were assessed by recycling the catalyst in consecutive photocatalytic

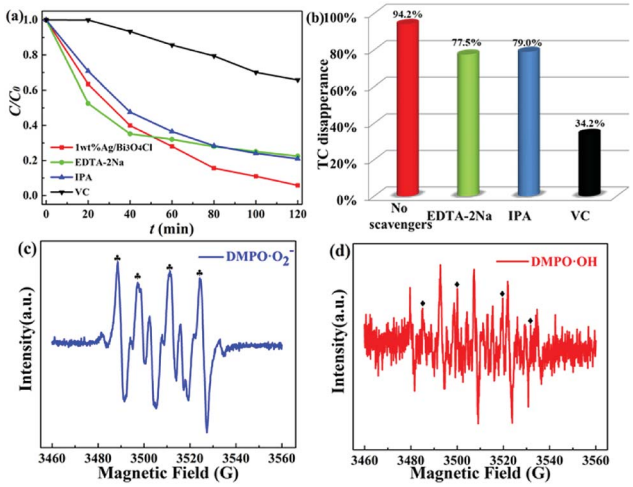

Fig. 8 (a and b) Active species trapping experiments for TC degradation over the 1.0 wt% Ag/Bi_3O_4Cl photocatalyst in the presence of different scavengers under visible light irradiation. ESR spectra of (c) DMPO-$^{\cdot}O_2^-$ in a methanol dispersion and (d) DMPO-$^{\cdot}$OH in an aqueous dispersion.

TC degradation experiments under visible light irradiation. As shown in Fig. 9a, there were no distinct changes in the photocatalytic degradation of TC over the 1.0 wt% Ag/Bi_3O_4Cl photocatalyst over five consecutive cycling experiments, which demonstrated the high photostability and recyclability of the as-prepared sample. Moreover, there was no obvious difference between the XRD pattern of the photocatalyst prior to any degradation experiments and that after five consecutive cycles (Fig. 9b), which further illustrated the splendid photostability and recyclability of the as-prepared nanocomposite.

In order to explain the charge separation process of the as-prepared photocatalyst, the valence band (VB) edge position and the conduction band (CB) edge position of Bi_3O_4Cl were calculated by using the following empirical formulas:[52]

$$E_{CB} = \chi - E^e - 0.5E_g \quad (1)$$

$$E_{VB} = E_{CB} + E_g \quad (2)$$

in which E_{VB} and E_{CB} are the VB and CB edge potentials, respectively; and χ, E^e and E_g are the absolute electronegativity of the semiconductor (6.08 eV), the energy of free electrons on the hydrogen scale (about 4.5 eV) and the band gap energy of the semiconductor (2.78 eV), respectively.[26] Therefore, the E_{CB} and E_{VB} of Bi_3O_4Cl nanosheets were calculated to be 0.19 eV and 2.97 eV. Notably, the VB potential of the Bi_3O_4Cl nanosheets was more positive than the redox potential of $OH^-/^{\cdot}OH$ (1.99 eV *vs.* NHE) and $H_2O/^{\cdot}OH$ (2.7 eV *vs.* NHE),[25] therefore the H_2O and OH^- were oxidized by h^+ into $^{\cdot}OH$ which played an oxidizing role in the TC degradation process.

Based on the aforementioned discussion and the experimental results, a possible mechanism for the degradation of TC by the Ag/Bi_3O_4Cl photocatalyst was proposed and is shown in Fig. 10. When the Ag/Bi_3O_4Cl photocatalyst is exposed to visible light, the electrons (e^-) in the VB of the Bi_3O_4Cl nanosheets can be excited to the CB, leaving holes (h^+) in the VB of the Bi_3O_4Cl nanosheets. The photogenerated holes remain in the VB of Bi_3O_4Cl nanosheets to directly oxidize OH^- or H_2O to form $^{\cdot}OH$ active species. However, the super-oxygen radical ($^{\cdot}O_2^-$) cannot be generated because the VB of the Bi_3O_4Cl nanosheets is more positive than the $O_2/^{\cdot}O_2^-$ potential (−0.046 eV *vs.* NHE).[25] Therefore, the existence of Ag nanoparticles is extraordinarily significant because the absorbance of the metallic Ag nanoparticles leads to the generation of abundant electron–hole pairs, as shown in Fig. 10. The photogenerated electrons (e^-) of Bi_3O_4Cl are transferred to the Ag nanoparticles and recombine with the plasmon-generated holes of the metallic Ag nanoparticles because the CB edge potential of Bi_3O_4Cl (0.19 eV *vs.* NHE) is more negative than the Fermi level of Ag (0.4 eV *vs.* NHE).[38] Subsequently, electrons (e^-) on the Ag nanoparticles can be captured by O_2 in water to generate $^{\cdot}O^{2-}$ radicals which are vigorous oxidants that can oxidize TC to its degradation products. Throughout the above analysis, the antibiotic is gradually damaged by the Ag/Bi_3O_4Cl photocatalyst; the degradation and charge carrier transfer processes can be described as follows:

$$Bi_3O_4Cl + h\nu \rightarrow Bi_3O_4Cl\ (h^+) + Bi_3O_4Cl\ (e^-) \quad (3)$$

$$H_2O \rightarrow H^+ + OH^- \quad (4)$$

$$h^+ + OH^- \rightarrow {}^{\cdot}OH \quad (5)$$

$$e^- + Ag \rightarrow Ag\ (e^-) \quad (6)$$

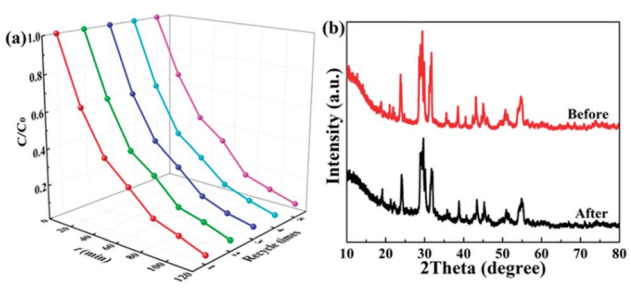

Fig. 9 (a) The TC degradation efficiency of the 1.0 wt% Ag/Bi_3O_4Cl photocatalyst under visible light irradiation over five cycles. (b) XRD patterns of the 1.0 wt% Ag/Bi_3O_4Cl photocatalyst before and after five cycles of photocatalytic degradation.

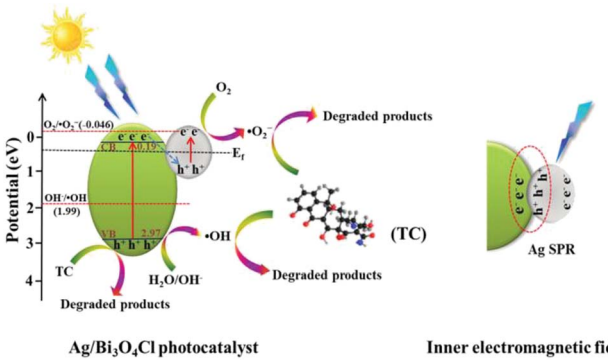

Fig. 10 The possible photocatalytic mechanism of the Ag/Bi_3O_4Cl photocatalyst in the degradation of TC under visible light irradiation.

$$O_2 + Ag\ (e^-) \rightarrow {}^{\bullet}O^{2-} + Ag \quad (7)$$

$${}^{\bullet}O^{2-}\ ({}^{\bullet}OH \text{ or } h^+) + TC \rightarrow \text{degradation products} \quad (8)$$

4. Conclusions

In summary, a novel Ag/Bi_3O_4Cl photocatalyst was successfully synthesized by a simple photodeposition process. The as-prepared Ag/Bi_3O_4Cl photocatalyst displayed significantly higher photocatalytic efficiency than bare Bi_3O_4Cl nanosheets for the degradation of TC under visible light irradiation. Among the photocatalyst specimens, the 1.0 wt% Ag/Bi_3O_4Cl sample showed the optimal photocatalytic activity, reaching 94.2% degradation of TC in 120 min under visible light irradiation. The rate constant of the 1.0 wt% Ag/Bi_3O_4Cl sample was 3.05-fold higher than that of the bare Bi_3O_4Cl nanosheets. The enhanced photocatalytic activity for the Ag/Bi_3O_4Cl photocatalyst could be due to the SPR absorbance of the metallic Ag nanoparticles. This work provides a new approach for synthesizing novel Ag/Bi_3O_4Cl photocatalysts and studying the possible mechanism of TC degradation.

Conflicts of interest

There are no conflicts to declare.

Author contributions

All the authors contributed to this work.

Acknowledgements

We would like to acknowledge the National Natural Science Foundation of China (21576112, 21546006 and 21606114), the Six Talent Peaks Project in Jiangsu Province (XNY-009), the Foundation Research Project of JiangSu Province (the Natural Science Fund BK20150536), Jiangsu Planned Projects for Postdoctoral Research Funds (1701025A) the Postdoctoral Science Foundation of China (2017M611712, 2017M611717) and the Talent Introduction Project of Jiangsu University (17JDG020).

References

1 X. X. Zhao, Z. Y. Lu, M. B. Wei, M. H. Zhang, H. J. Dong, C. W. Yi, R. Ji and Y. S. Yan, *Appl. Catal., B*, 2018, **220**, 137–147.
2 F. Chen, Q. Yang, J. Sun, F. B. Yao, S. N. Wang, Y. L. Wang, X. L. Wang, X. M. Li, C. G. Niu, D. B. Wang and G. M. Zeng, *ACS Appl. Mater. Interfaces*, 2016, **8**, 32887–32900.
3 L. W. Chen, X. Zuo, L. Zhou, Y. Huang, S. J. Yang, T. M. Cai and D. H. Ding, *Chem. Eng. J.*, 2018, **45**, 64–374.
4 H. B. Yu, B. B. Huang, H. Wang, X. Z. Yuan, L. B. Jiang, Z. B. Wu, J. Zhang and G. M. Zeng, *J. Colloid Interface Sci.*, 2018, **522**, 82–94.
5 F. L. Wang, Y. P. Feng, P. Chen, Y. F. Wang, Y. H. Su, Q. X. Zhang, Y. Q. Zeng, Z. J. Xie, H. J. Liu, Y. Liu, W. Y. Lv and G. G. Liu, *Appl. Catal., B*, 2018, **227**, 114–122.
6 Z. Zhu, Y. Yu, H. J. Dong, Z. Liu, C. X. Li, P. W. Huo and Y. S. Yan, *ACS Sustainable Chem. Eng.*, 2017, **5**, 10614–10623.
7 H. N. Che, G. B. Che, H. J. Dong, W. Hu, H. Hu, C. B. Liu and C. M. Li, *Appl. Surf. Sci.*, 2018, **455**, 705–716.
8 H. N. Che, G. B. Che, E. H. Jiang, C. B. Liu, H. J. Dong and C. M. Li, *J. Taiwan Inst. Chem. Eng.*, 2018, **91**, 224–234.
9 S. J. Li, S. W. Hu, W. Jiang, Y. P. Liu, Y. T. Zhou, Y. Liu and L. Y. Mo, *J. Colloid Interface Sci.*, 2018, **521**, 42–49.
10 S. X. Yu, Y. H. Zhang, F. Dong, M. Li, T. R. Zhang and H. W. Huang, *Appl. Catal., B*, 2018, **226**, 441–450.
11 R. Li, Y. F. Jia, J. Wu and Q. Zhen, *RSC Adv.*, 2015, **5**, 40764–40771.
12 R. B. Wei, Z. L. Huang, G. H. Gu, Z. Wang, L. X. Zeng, Y. B. Chen and Z. Q. Liu, *Appl. Catal., B*, 2018, **231**, 101–107.
13 C. B. Liu, P. Li, G. L. Wu, B. F. Luo, S. Lin, A. Ren and W. D. Shi, *RSC Adv.*, 2015, **5**, 33938–33945.
14 S. S. Ma, J. J. Xue, Y. M. Zhou and Z. W. Zhang, *RSC Adv.*, 2015, **5**, 40000–40006.
15 G. J. Wu, Y. Zhao, Y. W. Li, B. Souvanhthong, H. M. Ma and J. Z. Zhao, *Ceram. Int.*, 2018, **44**, 5392–5401.
16 X. Xiao, C. X. Zheng, M. L. Lu, L. Zhang, F. Liu, X. X. Zuo and J. M. Nan, *Appl. Catal., B*, 2018, **228**, 142–151.
17 B. Priya, P. Raizada, N. Singh, P. Thakur and P. Singh, *J. Colloid Interface Sci.*, 2016, **479**, 271–283.
18 F. Chen, H. W. Huang, Y. H. Zhang and T. R. Zhang, *Chin. Chem. Lett.*, 2017, **28**, 2244–2250.
19 S. B. Ning, L. Y. Ding, Z. G. Lin, Q. Y. Lin, H. L. Zhang, H. X. Lin, J. L. Long and X. X. Wang, *Appl. Catal., B*, 2016, **185**, 203–212.
20 J. Li, L. J. Cai, J. Shang, Y. Yu and L. Z. Zhang, *Adv. Mater.*, 2016, **28**, 4059–4064.
21 G. Hamscher, S. Sczesny, H. Hoper and H. Nau, *Anal. Chem.*, 2002, **74**, 1509–1518.
22 M. K. Lee, T. G. Kim, W. Kim and Y. M. Sung, *J. Phys. Chem. C*, 2008, **112**, 10079–10082.
23 W. Wang, M. Lai, J. J. Fang and C. H. Lu, *Appl. Surf. Sci.*, 2018, **439**, 430–438.
24 L. Tang, C. Y. Feng, Y. C. Deng, G. M. Zeng, J. J. Wang, Y. N. Liu, H. P. Peng and J. J. Wang, *Appl. Catal., B*, 2018, **230**, 102–114.
25 B. F. Luo, D. B. Xu, D. Li, G. L. Wu, M. M. Wu, W. D. Shi and M. Chen, *ACS Appl. Mater. Interfaces*, 2015, **31**, 17061–17069.
26 A. K. Chakraborty and M. A. Kebede, *React. Kinet., Mech. Catal.*, 2012, **106**, 83–98.
27 S. Senobari and A. Nezamzadeh-Ejhieh, *J. Mol. Liq.*, 2018, **261**, 208–217.
28 A. J. Anceno and R. M. Stuetz, *Appl. Catal., B*, 2016, **181**, 661–671.
29 H. N. Che, L. H. Liu, G. B. Che, H. J. Dong, C. B. Liu and C. M. Li, *Chem. Eng. J.*, 2019, **357**, 209–219.
30 A. Turki, C. Guillard, F. Dappozze, Z. Ksibi, G. Berhault and H. Kochkar, *Appl. Catal., B*, 2015, **163**, 404–414.
31 G. Q. Tan, L. N. She, T. Liu, C. Xu, H. J. Ren and A. Xia, *Appl. Catal., B*, 2017, **207**, 120–133.

32 Z. Zhu, Z. Y. Lu, D. D. Wang, X. Tang, Y. S. Yan, W. D. Shi, Y. S. Wang, N. L. Gao, X. Yao and H. J. Dong, *Appl. Catal., B*, 2016, **182**, 115–122.
33 F. A. Sofi, K. Majid and O. Mehraj, *J. Alloys Compd.*, 2018, **737**, 798–808.
34 C. Liu, H. J. Zhu, Y. S. Zhu, P. Y. Dong, H. J. Hou, Q. X. Xu, X. W. Chen, X. G. Xi and W. H. Hou, *Appl. Catal., B*, 2018, **228**, 54–63.
35 D. M. Ma, J. B. Zhong, J. Z. Li, L. Wang and R. F. Peng, *Appl. Surf. Sci.*, 2018, **443**, 497–505.
36 L. Xu, F. X. Bu, M. Hu, C. Y. Jin, D. M. Jiang, Z. J. Zhao, Q. H. Zhang and J. S. Jiang, *Chem. Commun.*, 2014, **50**, 13849–13852.
37 Z. Zhu, X. Tang, C. C. Ma, M. S. Song, N. L. Gao, Y. S. Wang, P. W. Huo, Z. Y. Lu and Y. S. Yan, *Appl. Surf. Sci.*, 2016, **387**, 366–374.
38 J. B. Chen, H. N. Che, K. Huang, C. B. Liu and W. D. Shi, *Appl. Catal., B*, 2016, **192**, 134–144.
39 W. J. Liu, X. B. Liu, Y. H. Fu, Q. Q. You, R. K. Huang, P. Liu and Z. H. Li, *Appl. Catal., B*, 2012, **123**, 78–83.
40 D. Wei, F. Tian, Z. Lu, H. Yang and R. Chen, *RSC Adv.*, 2016, **6**, 52264–52270.
41 C. Wang, X. Zhang and X. Song, *ACS Appl. Mater. Interfaces*, 2016, **8**, 5320–5326.
42 M. Shakeel, B. S. Li, M. Arif, G. Yasin, W. Rehman, A. U. Khan, S. Khan, A. Khan and J. Ali, *Appl. Catal., B*, 2018, **227**, 433–445.
43 H. N. Che, C. B. Liu, W. Hu, H. Hu, J. Q. Li, J. Y. Dou, W. D. Shi, C. M. Li and H. J. Dong, *Catal. Sci. Technol.*, 2018, **8**, 622–631.
44 N. Sobana, M. Muruganadham and M. Swaminathan, *J. Mol. Catal. A: Chem.*, 2006, **258**, 124–132.
45 N. Spataru, C. Anastasescu, M. M. Radu, I. Balint, C. Negrila, T. Spataru and A. Fujishima, *Appl. Surf. Sci.*, 2018, **444**, 216–223.
46 M. Wang, P. Y. Guo, Y. Zhang, C. M. Lv, T. Y. Liu, T. Y. Chai, Y. H. Xie, Y. Z. Wang and T. Zhu, *J. Hazard. Mater.*, 2018, **349**, 224–233.
47 S. F. Kang, W. Huang, L. Zhang, M. F. He, S. Y. Xu, D. Sun and X. Jiang, *ACS Appl. Mater. Interfaces*, 2018, **10**, 13796–13804.
48 A. Shanaghi, H. Nonahal and P. K. Chu, *J. Alloys Compd.*, 2018, **739**, 92–100.
49 J. Shen, D. H. Chen, W. Zhao and W. W. Zhang, *ChemistrySelect*, 2018, **3**, 3363–3373.
50 H. Zhao, X. S. Wang, J. F. Feng, Y. N. Chen, X. Yang, S. Y. Gao and R. Cao, *Catal. Sci. Technol.*, 2018, **8**, 1288–1295.
51 H. Xu, J. Xie, W. Jia, G. M. Wu and Y. L. Cao, *J. Colloid Interface Sci.*, 2018, **516**, 511–521.
52 F. Deng, L. N. Zhao, X. B. Luo, S. L. Luo and D. D. Dionysiou, *Chem. Eng. J.*, 2018, **333**, 423–433.